Applied Catalysis B: Environmental 91 (2009) 524–532

Contents lists available at ScienceDirect

Applied Catalysis B: Environmental

journal homepage: www.elsevier.com/locate/apcatb

High temperature steam reforming of methanol over $Cu/ZnO/ZrO_2$ catalysts

Yasuyuki Matsumura [a,*], Hideomi Ishibe [b]

[a] National Institute of Advanced Industrial Science and Technology (AIST), Kansai Center, Midorigaoka, Ikeda, Osaka 563-8577, Japan
[b] Nippon Seisen Co., Ltd., Hirakata Plant, Ikenomiya, Hirakata, Osaka 573-8522, Japan

ARTICLE INFO

Article history:
Received 20 February 2009
Received in revised form 1 June 2009
Accepted 22 June 2009
Available online 26 June 2009

Keywords:
Methanol steam reforming
$Cu/ZnO/ZrO_2$
Hydrogen production
Stability
TEM
XRD
XPS

ABSTRACT

Methanol steam reforming to hydrogen and carbon dioxide is catalyzed at 400 °C over $Cu/ZnO/ZrO_2$ (Cu content, 30 wt.%) prepared by a coprecipitation method. Conventional binary catalysts of Cu/ZnO and Cu/ZrO_2 have also been prepared by the same method. The activity of $Cu/ZnO/ZrO_2$ is stable in comparison with the binary catalysts and a commercial $Cu/ZnO/Al_2O_3$. The selectivity to carbon monoxide by-produced over $Cu/ZnO/ZrO_2$ is fairly low. The particle sizes of Cu and ZnO for $Cu/ZnO/ZrO_2$ are significantly smaller than those for Cu/ZnO, and the BET surface area of $Cu/ZnO/ZrO_2$ is 2–3 times as high as that of Cu/ZnO. The Cu particle size of $Cu/ZnO/ZrO_2$ is stable during the reaction, but growth of ZnO and ZrO_2 particles is accompanied with the deactivation.

1. Introduction

Polymer electrolyte fuel cells (PEFCs) have been regarded as compact and efficient power generators for stationary and mobile applications. Hydrogen is the most potential fuel for PEFCs, but there are problems in its storage.

Methanol is a capable feedstock of hydrogen processors for fuel cells. Selective methanol steam reforming is usually carried out below 300 °C over copper catalysts such as $Cu/ZnO/Al_2O_3$ for hydrogen production. Since the catalysts are easily deactivated and less selective (by-production of unfavorable carbon monoxide) at the higher temperature, the reactor cannot be directly heated with combustion gas; therefore, thermal oil is usually employed for the heat supply [1]. This is an obstacle in development of a simple and compact hydrogen processor. In addition, the activity of the conventional catalyst is insufficient for the compact reformer. For example, Choi and Stenger reported that no complete conversion of methanol can be attained over a commercial $Cu/ZnO/Al_2O_3$ at 250 °C with the GHSV as small as 1100 h^{-1} [2]. High operation temperature will realize the direct heat supply and large heat flux to the reactor. The reaction rate is generally large at high temperatures and it will also contribute to the compact reformer. Hence, a new active catalyst durable at the high temperature is required for the efficient reactor.

Removal of carbon monoxide is another problem in the hydrogen processor. The hydrogen fuel for PEFCs must not contain carbon monoxide above 10 ppm, which poisons the catalytic anode [3]. Selective oxidation of carbon monoxide is often carried out to remove carbon monoxide to the level less than 10 ppm [4], but an excessive amount of oxygen is required in the process and it consumes hydrogen. The CO selectivity is usually increased at the high reaction temperature. Membrane reactors comprised of hydrogen separation membranes and reforming catalysts are proposed for the production of pure hydrogen from methanol [5–10] and it is a solution for removal of carbon monoxide. Han et al. reported the thermal efficiency of the membrane reactor as high as 82% at 350 °C [11]. Although palladium membranes are the most promising on the viewpoint of the hydrogen permeability and selectivity, the formation of β-Pd hydride is a risk to damage the membrane at the operation temperature less than 300 °C [12]. In addition, the permeability at 300 °C is ca. 60% of that at 400 °C when the activation energy is 15 kJ mol^{-1} [13]. Thus, the operation temperature of the membrane reactor should be higher than 300 °C, and it meets the requirement of the compact reformer that we are going to integrate with the membrane. Catalysts containing transition metals such as nickel and iridium mainly produce hydrogen and carbon monoxide in the reforming at around 400 °C [14,15]. While pure hydrogen is obtained through a pinhole-free membrane, defects usually exist on thin membranes and they decrease the selectivity ratio of hydrogen to other gases and result in contamination of hydrogen with carbon monoxide. Thus, the by-production of carbon monoxide is unfavorable even

* Corresponding author. Fax: +81 72 751 9623.
E-mail address: yasu-matsumura@aist.go.jp (Y. Matsumura).

0926-3373/$ – see front matter © 2009 Elsevier B.V. All rights reserved.
doi:10.1016/j.apcatb.2009.06.023

if the hydrogen purification is carried out with the palladium membrane.

The ternary system of $Cu/ZnO/ZrO_2$ was first developed for the methanol synthesis from hydrogen and carbon dioxide [16–19]. Agrell et al. reported methanol steam reforming on Cu(32 wt.%)/ZnO(40 wt.%)/ZrO_2 at temperatures less than 300 °C [20]. By-production of carbon monoxide was significantly small in comparison with Cu/ZnO or $Cu/ZnO/Al_2O_3$, and the activity was appreciably high. Matter et al. reported that the activity of Cu(29 wt.%)/ZnO(28 wt.%)/ZrO_2 was the highest at 300 °C or below among the catalysts examined by them [21]. Since the selectivity to carbon monoxide usually increases with an increase in the reaction temperature, suppression of CO formation is important in the high temperature reforming above 300 °C as well as the durability of the catalyst.

In the present work, we examined the activity of copper catalysts with the Cu content of 30 wt.% to find the promising catalysts durable at 400 °C. It is shown that $Cu/ZnO/ZrO_2$ is fairly stable with a low CO selectivity in comparison with conventional catalysts such as Cu/ZnO, Cu/ZrO_2, and $Cu/ZnO/Al_2O_3$.

2. Experimental

A series of copper-based catalysts were prepared by coprecipitation from a 0.5-M aqueous mixture of $Cu(NO_3)_2{\cdot}3H_2O$ (Wako Pure Chemical, S grade), $Zn(NO_3)_2{\cdot}6H_2O$ (Wako, S), and/or $ZrO(NO_3)_2{\cdot}2H_2O$ (Wako, 1st) with addition of an aqueous solution of Na_2CO_3 (0.5 M) under vigorous stirring at 80 °C. After filtration, the precipitate was dispersed in distilled water and washed at room temperature for ca. 0.5 h. The procedure was repeated for several times until the pH value and conductivity of the filtrate reached to the levels of the distilled water. The precipitate was dried at 120 °C for 15 h and finally calcined in air at 500 °C for 12 h. The Cu content of the catalysts in the reduced form was always 30 wt.% and the catalysts will be referred as Cu/ZnO, Cu/ZrO_2 and $Cu/ZnO/xZrO_2$, where x represents the ZrO_2 content in wt.%. Here, the ZnO content will be $(70 - x)$ wt.%. A commercially available $Cu/ZnO/Al_2O_3$ catalyst (Süd-Chemie MDC-3) was also used as a reference.

Catalytic tests were performed in a fixed-bed continuous-flow reactor operated under atmospheric pressure. Zirconia balls (1 mm in diameter) were mixed with a powder catalyst (50–100 mesh) in order to reduce back pressure during the reaction and keep sufficient length of the catalyst layer (2.0 g in total of the catalyst and the balls). The mixture was placed in a tubular reactor made of stainless steel (i.d., 7 mm) with quartz-wool plugs. The catalyst was reduced with a reaction mixture of methanol, steam, and argon (1.0/1.2/0.5 in molar ratio) with a flow rate of 0.48 $dm^3\ min^{-1}$ at 250 °C for 1 h; then the reactor was heated up to 400 °C in the reaction flow. The effluent gas was dried with a cold trap at ca. −50 °C, and analyzed with an on-stream gas chromatograph (Shimadzu GC-8A; activated carbon, 2 m; Ar carrier) equipped with a thermal conductivity detector. The methanol conversion was determined from the material balance of the reactant and the products. The error was within 5%. No formation of formaldehyde, methane or methyl formate was observed. The reaction was reproducible within the error of 3%.

The structures of the catalysts after reduction with hydrogen at 250 °C for 1 h were evaluated by transmission electron microscopy (TEM) and high-angle annular dark field imaging in scanning transmission electron microscopy (HAADF/STEM) with energy dispersed X-ray spectroscopic (EDS) analysis using an FEI Tecnai G2 F20 Twin with an EDX detecting unit (EDAX Inc.) at the acceleration voltage of 200 kV.

Powder X-ray diffraction (XRD) patterns of the catalysts were recorded in air at room temperature with an MAC Science MP6XCE diffractometer using nickel-filtered Cu Kα radiation.

X-ray photoelectron spectra (XPS) were recorded at room temperature with a JEOL JPS-9010MX spectrometer (Al Kα). After the reaction the catalyst sample was taken out from the reactor after cooling under an argon stream for 12 h or longer and mounted in air to a sample holder. Since the sample was gradually oxidized in air, argon sputtering (400 V, 7 mA) was carried out for 5 s to remove oxygen adsorbed on the surface. Binding energies were corrected by the reference of the C 1s line at 284.6 eV. The surface atomic concentrations of Cu, Zn, Zr, and O were calculated from the peak areas using the atomic relative sensitivity factors (ARSF) of Cu $2p_{3/2}$ (5.8), Zn $2p_{3/2}$ (8.1), Zr 3d (1.4), and O 1s (1.0) determined by measuring standard materials of Cu, Zn, and Zr metal plates and a quartz glass plate.

The BET surface areas of the catalysts were determined from the isotherms of nitrogen physisorption.

3. Results

3.1. High temperature steam reforming of methanol over conventional catalysts

Steam reforming of methanol was carried out over a commercial $Cu/ZnO/Al_2O_3$ catalyst at 400 °C for 420 min. The methanol conversion decreased with an increase in a time period of the reaction (Fig. 1). The selectivity to carbon monoxide increased gradually from 5.8% to 7.7%. On the other hand, the CO selectivity produced with Cu/ZnO decreased to 4.4% after 420-min on-stream and the methanol conversion was always higher than that of $Cu/ZnO/Al_2O_3$ by ca. 10%. The activity of Cu/ZrO_2 decreased steeply at the initial stage of the reaction. It should be noted that the CO selectivity was as low as 3.0% at 20-min on-stream, but it increased to 17.5% at the end of the reaction.

3.2. High temperature reforming over $Cu/ZnO/ZrO_2$

A part of zinc oxide in Cu/ZnO was replaced with zirconium oxide and the catalytic activity was examined at 400 °C. The initial activity of $Cu/ZnO/ZrO_2$ whose ZrO_2 content was 40 wt.% or below was similar to that of Cu/ZnO, but the methanol conversion at the end of the 1st reaction for 420 min was no less than 70% and significantly higher than that of the latter (cf. Figs. 1 and 2). When

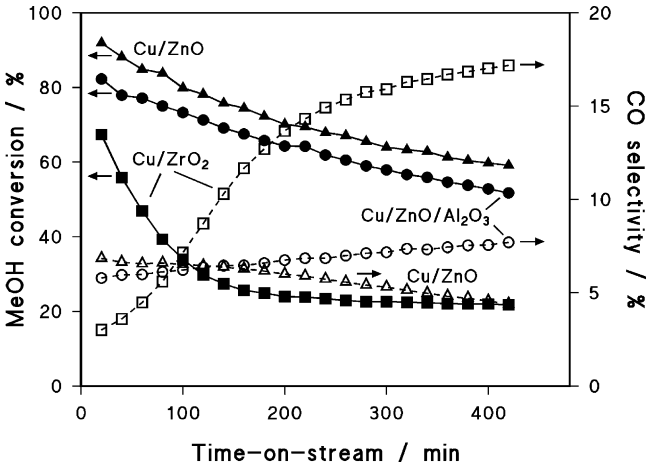

Fig. 1. Catalytic activity of conventional copper catalysts in methanol steam reforming at 400 °C. F/W, 1.6 $dm^3\ min^{-1}\ g^{-1}$. Circle symbols, $Cu/ZnO/Al_2O_3$; triangle, Cu/ZnO; square, Cu/ZrO_2.

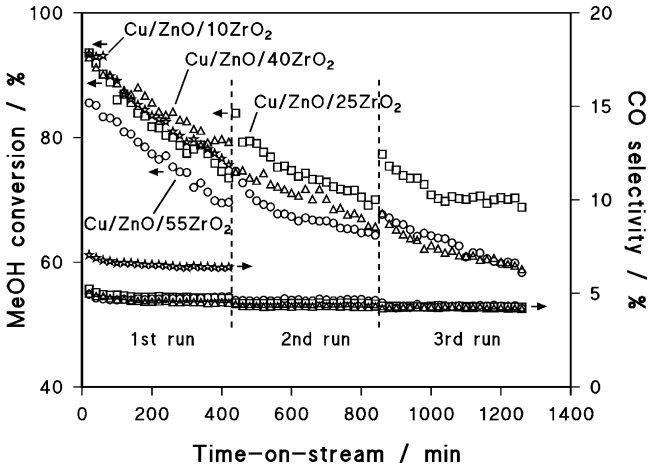

Fig. 2. Catalytic activity of $Cu/ZnO/ZrO_2$ in methanol steam reforming at 400 °C. F/W, 1.6 $dm^3\ min^{-1}\ g^{-1}$. Star symbols, $Cu/ZnO/10ZrO_2$; square, $Cu/ZnO/25ZrO_2$; triangle, $Cu/ZnO/40ZrO_2$; circle, $Cu/ZnO/55ZrO_2$.

the ZrO_2 content was 25 wt.% or above, the CO selectivity at 20-min on-stream was significantly smaller than that for Cu/ZnO.

After the reaction for 420 min, the catalyst was cooled to room temperature under an argon stream; then, the reaction was restarted at 400 °C after heating at 500 °C for 60 min in the argon stream. The activity of $Cu/ZnO/55ZrO_2$ was gradually decreased by the repetition of the reaction (see Fig. 2). The methanol conversion was decreased to 60% after the 3rd run. The activity of $Cu/ZnO/40ZrO_2$ was higher than that of $Cu/ZnO/55ZrO_2$ in the 1st run, but those of the 2nd and 3rd runs were almost the same as in the corresponding runs with $Cu/ZnO/55ZrO_2$. The activity of $Cu/ZnO/25ZrO_2$ in the end of the 2nd run was smaller than that in the 1st run, but that in the 3rd run was similar to that in the 2nd run. Although the pretreatment at 500 °C was aimed to give the catalyst the thermal impact accompanied with DSS (daily start and stop) operation, the initial activities of the 2nd and 3rd runs were higher than the final activities of the previous runs. The similar tendency was observed in the runs with the other $Cu/ZnO/ZrO_2$ catalysts. No increase in the initial activity of $Cu/ZnO/25ZrO_2$ in the 2nd run was observed in a different reaction without the pretreatment at 500 °C while the activity of the 2nd run decreased gradually to the level of the final activity with an increase in time-on-stream.

The activity of $Cu/ZnO/40ZrO_2$ was examined with different F/W values by changing the amount of the catalyst (0.20, 0.30, and 0.45 g). The CO selectivity and the methanol conversion decreased with an increase in the F/W (Fig. 3).

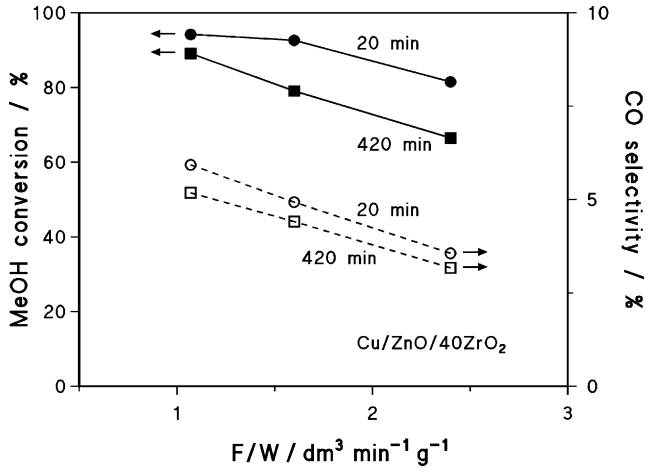

Fig. 3. Effect of F/W on catalytic activity of $Cu/ZnO/40ZrO_2$ at 400 °C in the 1st run. Circle symbols, 20-min on-stream; square, 420-min on-stream.

The methanol conversion of $Cu/ZnO/40ZrO_2$ at 300 °C was 84% with the CO selectivity of 1.6% under a reaction flow of methanol, steam, and argon (1.0/1.2/0.9) with F/W of 0.9 $dm^3\ min^{-1}\ g^{-1}$ while that for $Cu/ZnO/Al_2O_3$ was 80% with the selectivity of 3.0%.

3.3. TEM and HAADF/STEM analyses of the copper catalysts

The TEM image of Cu/ZnO reduced with hydrogen at 250 °C showed that the catalyst consisted of lumps whose size was mainly 30–50 nm and the lumps were highly aggregated (Fig. 4a). On a lump in Fig. 4b, Zn was mainly detected at point 1 in the HAADF/STEM image (Fig. 4c) by EDX analysis (Fig. 4d), but Cu was also present at point 2.

Amorphous-like portions were seen in the TEM image of Cu/ZrO_2 (Fig. 5a) and small particles with the size of ca. 10 nm existed in the portions which were not amorphous-like (Fig. 5b). On the points 1 and 2 in the HAADF/STEM image (Fig. 5c), Cu and Zr were present while Zr was not detected on the points 3 and 4 (Fig. 5d).

The particles in $Cu/ZnO/25ZrO_2$ were highly aggregated and different structures were observed in an aggregation of $Cu/ZnO/25ZrO_2$. That is, Cu and Zn were mainly present on a brim of an aggregation (Fig. 6) and amorphous-like structures containing Cu, Zn, and Zr were also observed in the same aggregation (Fig. 7). The TEM image of $Cu/ZnO/40ZrO_2$ was similar to that of Fig. 7 and Zn usually coexists with Zr (not shown).

3.4. X-ray diffraction of the catalyst

Peaks at 35.5°, 38.8°, and 48.7° in 2θ attributed to CuO were recorded with peaks attributed to ZnO in the XRD pattern for Cu/ZnO as prepared (Fig. 8a) [22]. The mean crystallite size of CuO was calculated to be 21 nm from the line broadening at 38.8° using Scherrer equation [23], assuming overlapping of two equivalent peaks [Cu(−1 1 1) and Cu(1 1 1)] with the separation of 0.21° [22]. The peaks at 43.4° and 50.6° attributed to Cu metal were recorded in the XRD pattern of a different aliquot of the catalyst taken out after the reforming at 400 °C for 20 min (Fig. 8b) [22]. The mean crystallite size of ZnO was calculated as 22 nm from the peak at 31.8° and that of Cu was 20 nm. The size of Cu after the reaction for 420 min was 21 nm, but the size of ZnO increased to 27 nm (Fig. 8c). The pattern for Cu/ZnO reduced with hydrogen at 250 °C

Table 1
Mean crystallite sizes of the catalysts after the reaction at 400 °C. The sizes were determined from the XRD peaks of Cu(1 1 1), Zn(1 0 0), and ZrO_2(1 1 1).

Catalyst	Time-on-stream/min	Mean crystallite size/nm		
		Cu	ZnO	ZrO_2
Cu/ZnO	20	20	22	–
Cu/ZnO	420	21	27	–
Cu/ZnO	Reduced[a]	18	24	–
$Cu/ZnO/10ZrO_2$	20	14	14	10
$Cu/ZnO/10ZrO_2$	420	16	15	10
$Cu/ZnO/25ZrO_2$	20	16	14	9
$Cu/ZnO/25ZrO_2$	420	17	14	8
$Cu/ZnO/25ZrO_2$	420 × 3	16	14	10
$Cu/ZnO/25ZrO_2$	Reduced[a]	13	14	–
$Cu/ZnO/40ZrO_2$	20	18	13	3
$Cu/ZnO/40ZrO_2$	420	16	14	3
$Cu/ZnO/40ZrO_2$	420 × 3	18	18	10
$Cu/ZnO/55ZrO_2$	20	18	12	4
$Cu/ZnO/55ZrO_2$	420	19	12	6
$Cu/ZnO/55ZrO_2$	420 × 3	19	17	12
Cu/ZrO_2	20	29	–	13
Cu/ZrO_2	420	29	–	15
Cu/ZrO_2	Reduced[a]	27	–	12

[a] Just after reduction with hydrogen at 250 °C for 1 h.

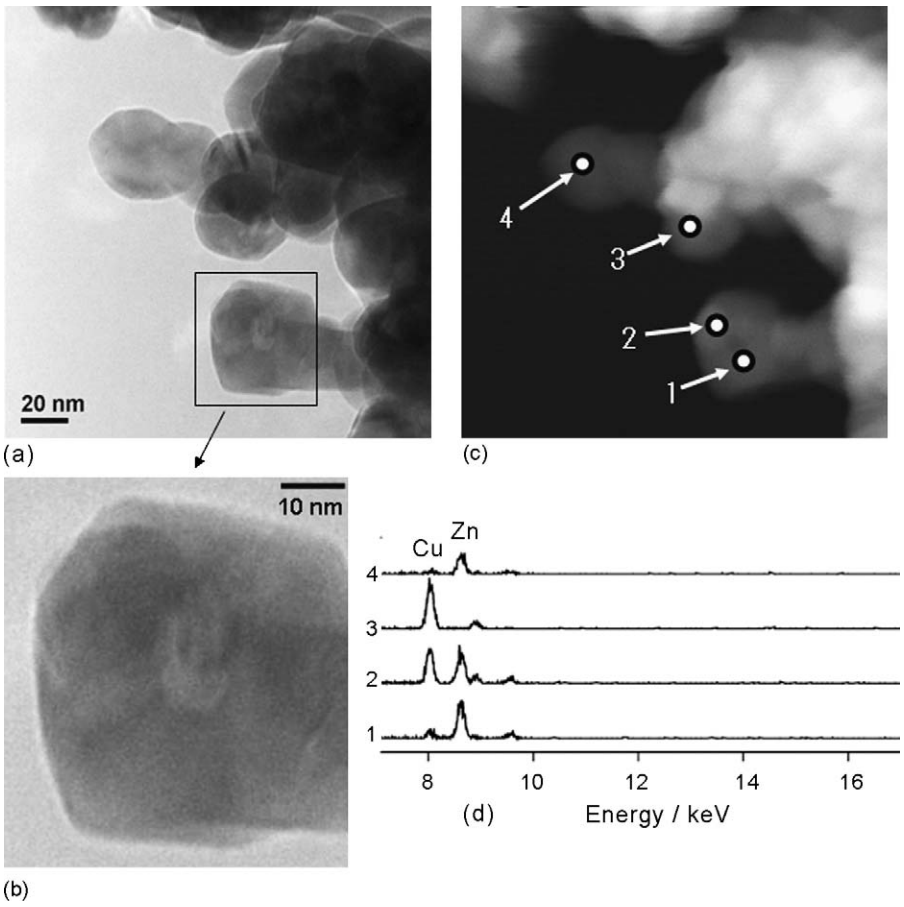

Fig. 4. TEM and HAADF/STEM images and EDS analysis of Cu/ZnO reduced with hydrogen at 250 °C for 1 h. (a) TEM image, (b) partial enlargement of the TEM image, (c) HAADF/STEM image, and (d) EDS spectra on points 1–4.

for 1 h was similar to that after the reforming at 400 °C for 20 min (cf. Fig. 8b and d). The mean crystallite sizes for the catalysts were summarized in Table 1.

The XRD peaks attributed to CuO were also recorded in the pattern of Cu/ZrO_2 as prepared. The peak intensity was weak and the mean crystallite size was calculated to be 14 nm (Fig. 9a). The peak at 30.5° attributed to tetragonal ZrO_2(1 1 1) [22] was present with a broad diffraction pattern which is similar to that of amorphous ZrO_2 [24]. The peaks attributed to Cu metal appeared with clear peaks attributed to tetragonal ZrO_2 in the pattern of the catalyst after the reaction for 20 min (Fig. 9b). The mean crystallite size of ZrO_2 was calculated as 13 nm from the peak at 30.3° and that of Cu was 28 nm (see Table 1). The peak intensities for Cu and ZrO_2 increased after the reaction for 420 min (Fig. 9c). The shoulder at ca. 34° can be attributed to monoclinic ZrO_2 [22]. After the reduction with hydrogen at 250 °C, the peaks attributed to Cu metal existed with the peak for ZrO_2 at 30.5° overlapped with a broad diffraction pattern (Fig. 9d).

The peak at 30–31° attributed to tetragonal ZrO_2 was broad and weak in the XRD pattern for Cu/ZnO/55ZrO_2 as prepared (Fig. 10a). The peak was unclear in the patterns of Cu/ZnO/40ZrO_2 (Fig. 11a) and Cu/ZnO/25ZrO_2 (Fig. 12a). Addition of zirconium oxide to Cu/ZnO decreased the mean crystallite size of CuO to 11–12 nm regardless of the ZrO_2 content. The mean crystallite size of ZnO was also decreased by the addition of zirconium oxide, that is, the sizes were 14 nm for 10 wt.% ZrO_2, 12 nm for 25 wt.% and 40 wt.%, and 9 nm for 55 wt.%. After the reaction for 20 min, the peaks for Cu metal appeared (e.g., Figs. 10b, 11b, and 12b) and the mean crystallite sizes were 14–19 nm, which were considerably smaller than that for Cu/ZnO or Cu/ZrO_2 (see Table 1). The size of Cu was kept even after the reactions for 3 times. The crystallite sizes of ZnO for Cu/ZnO/10ZrO_2 and Cu/ZnO/25ZrO_2 after the reaction for 20 min were similar to those for the samples as prepared and the size for Cu/ZnO/25ZrO_2 was kept after the reactions for 3 times. The sizes of ZnO for Cu/ZnO/40ZrO_2 and Cu/ZnO/55ZrO_2 after the reaction for 420 min were almost the same as those after the reaction for 20 min, but the sizes after the 3rd runs were significantly larger.

The peaks for ZrO_2 were broad in the patterns of Cu/ZnO/55ZrO_2 and Cu/ZnO/40ZrO_2 after the reaction for 420 min (Figs. 10c and 11c), but they became sharp after the 3rd runs (Figs. 10d and 11d). The intensity of the peaks attributed to ZrO_2 for Cu/ZnO/25ZrO_2 increased gradually with the time period of the reaction (Fig. 12b–d). After the reduction of Cu/ZnO/25ZrO_2 with hydrogen at 250 °C, the peaks attributed to Cu metal and ZnO were present (Fig. 12e). The peaks for ZrO_2 were unclear.

3.5. XPS of the copper catalysts

The surface composition of the copper catalyst was analyzed by XPS. No peaks attributed to copper oxides were recorded in the XRD patterns for the catalysts taken out from the reactor after the reaction; however, the XPS of Cu $2p_{3/2}$ was a typical spectrum of CuO with a shake-up line (not shown) [25], appearing that the surface of the catalyst was oxidized during the handling in air. Hence, the detection of the electronic state of copper on the used catalyst was difficult and we only evaluated the surface composition of the sample after removal of the surface oxygen layer by argon sputtering (Table 2). The binding energy of Cu $2p_{3/2}$ was 932.0–932.7 eV regardless of the samples, while no shake-up line was observed. The kinetic energy of Cu L_3VV (Auger line) was

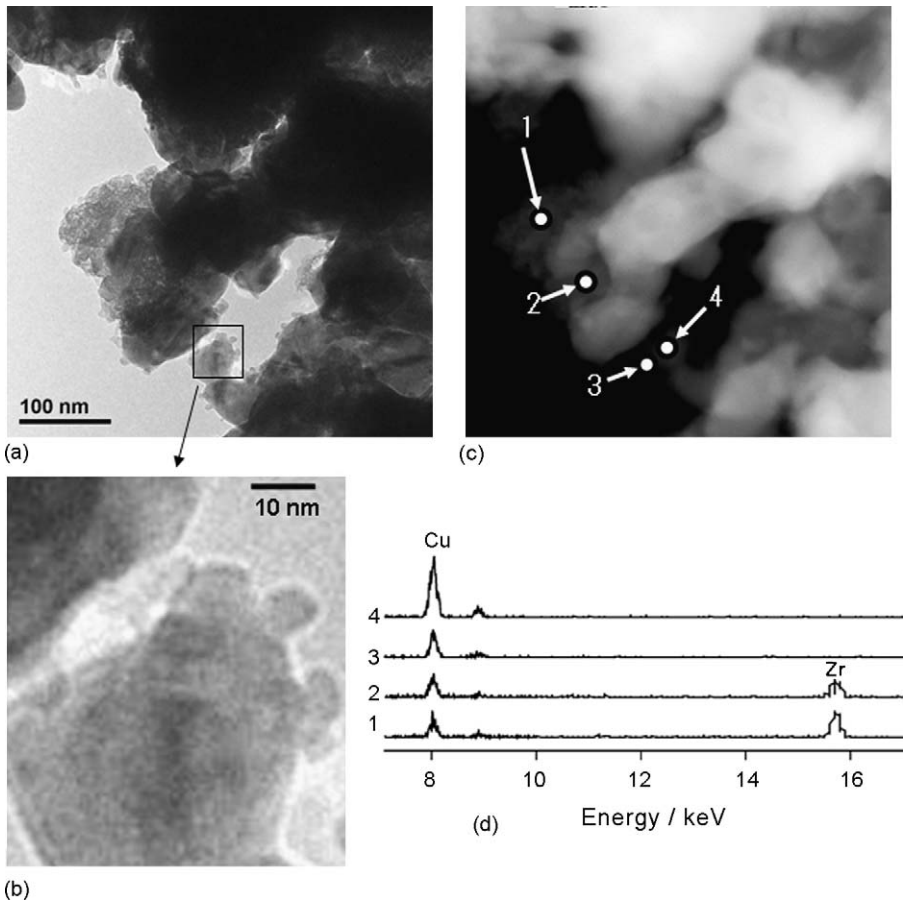

Fig. 5. TEM and HAADF/STEM images and EDS analysis of Cu/ZrO_2 reduced with hydrogen at 250 °C for 1 h. (a) TEM image, (b) partial enlargement of the TEM image, (c) HAADF/STEM image, and (d) EDS spectra on points 1–4.

918.0–919.5 eV and the α value (Auger parameter + photon energy) was 1850.5–1851.5 eV, showing copper on the surface was reduced to metal by the sputtering; it is known that the α value for Cu and Cu_2O are 1851.3 and 1849.4 eV, respectively [26]. The binding energies were 1021.6–1022.0 eV for Zn $2p_{3/2}$ (except Cu/ZrO_2), 182.2–182.5 eV for Zr $3d_{5/2}$ (except Cu/ZnO), and 529.8–530.8 eV for O 1s regardless of the samples, showing that ZnO and/or ZrO_2 are not reduced on the surface [26].

The surface atomic concentration of Zr^{4+} increased with an increase in the ZrO_2 content of the catalysts and that of Zn^{2+} decreased reversely (see Table 2). The Cu concentration is fairly stable at around 10% regardless of the samples.

3.6. BET surface area of the copper catalysts

The BET surface area of Cu/ZnO after the reaction for 20 min was 20 $m^2\ g^{-1}$, and it decreased to 14 $m^2\ g^{-1}$ after the reaction for 420 min (see Table 2). The areas of $Cu/ZnO/ZrO_2$ after the reaction for 420 min were also smaller than those after the reaction for 20 min, while the values were significantly higher than that for

Table 2
Surface atomic concentrations determined by XPS and surface areas of the catalysts after the reaction at 400 °C.

Catalyst	Time-on-stream/min	Surface atomic concentration/%			BET surface area/$m^2\ g^{-1}$	Cu surface area[a]/$m^2\ g^{-1}$
		Cu	Zn^{2+}	Zr^{4+}		
Cu/ZnO	20	10	29	0	20	2
Cu/ZnO	420	14	32	0	14	2
$Cu/ZnO/10ZrO_2$	20	10	27	10	53	6
$Cu/ZnO/10ZrO_2$	420	10	22	11	47	5
$Cu/ZnO/25ZrO_2$	20	9	22	17	43	5
$Cu/ZnO/25ZrO_2$	420	10	20	16	31	4
$Cu/ZnO/25ZrO_2$	420 × 3	10	24	8	34	4
$Cu/ZnO/40ZrO_2$	20	9	16	21	55	6
$Cu/ZnO/40ZrO_2$	420	12	15	18	46	6
$Cu/ZnO/40ZrO_2$	420 × 3	11	13	20	48	6
$Cu/ZnO/55ZrO_2$	20	8	11	29	56	5
$Cu/ZnO/55ZrO_2$	420	11	6	26	44	6
$Cu/ZnO/55ZrO_2$	420 × 3	14	6	32	39	6
Cu/ZrO_2	20	12	0	32	26	3
Cu/ZrO_2	420	12	0	35	30	4

[a] The area was determined from the surface atomic concentration and BET surface area.

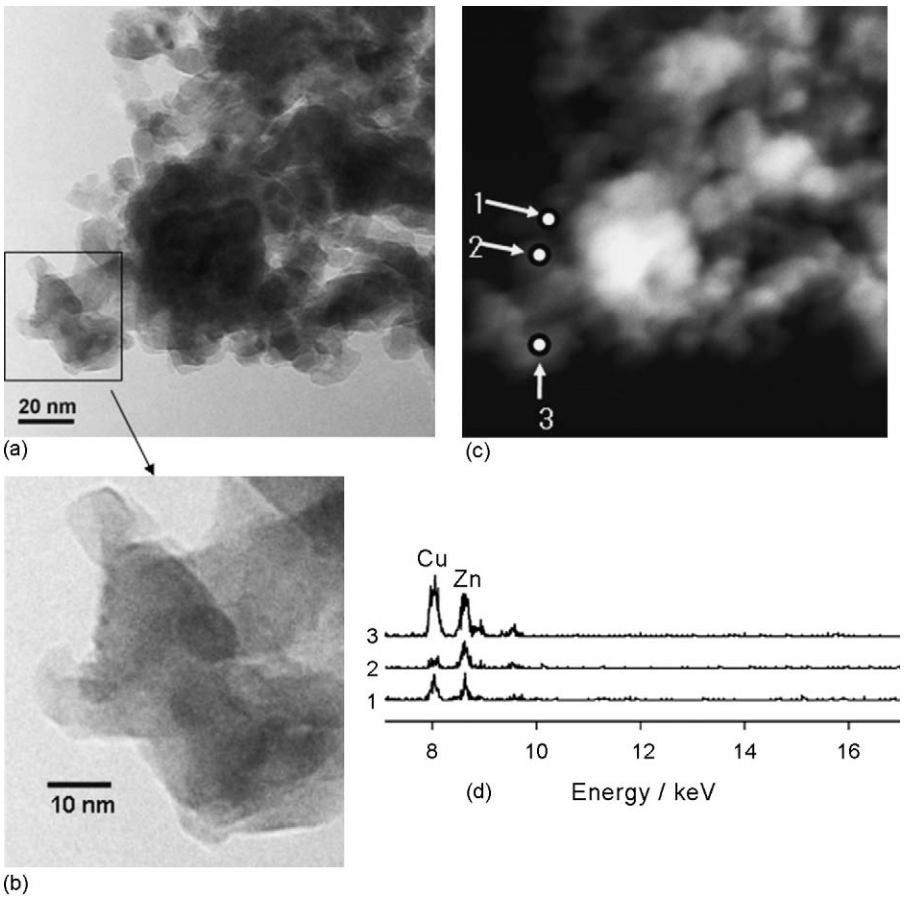

Fig. 6. TEM and HAADF/STEM images and EDS analysis of Cu/ZnO/25ZrO_2 reduced with hydrogen at 250 °C for 1 h. (a) TEM image, (b) partial enlargement of the TEM image, (c) HAADF/STEM image, and (d) EDS spectra on points 1–3.

Cu/ZnO. The areas after the reactions for 3 times were similar to those after the 1st runs.

4. Discussion

4.1. Deactivation of Cu/ZnO

Carbon monoxide is considered as a secondary product of the steam reforming of methanol over Cu/ZnO/Al_2O_3 by the reverse water gas-shift (WGS) reaction ($CO_2 + H_2 \rightarrow CO + H_2O$) [27,28]. In this mechanism CO production is suppressed when methanol conversion is low. However, the CO selectivity increased gradually during the reaction with a commercial Cu/ZnO/Al_2O_3 catalyst at 400 °C despite decrease in the methanol conversion (see Fig. 1). Hence, it is supposed that the nature of the active sites changes during the high temperature reaction. Decomposition of methanol is a possible mechanism of CO by-production [2,29,30]. Formation of the new sites being active to the decomposition would increase the CO selectivity. In the case of Cu/ZnO, no such phenomenon was observed during the reforming at 400 °C, implying that alumina is involved in the deactivation mechanism for Cu/ZnO/Al_2O_3.

Evaluation of Cu surface area is usually determined by the surface oxidation with N_2O, but we estimated the Cu surface area from the surface atomic concentrations and the BET surface area (see Table 2) due to the quantitative limitation of the catalysts recovered from the reactor. That is, the surface area of Cu (S_{Cu}) is calculated by the equation, $S_{Cu} = S_{BET} \times c_{Cu}/d_{Cu}/(c_{Cu}/d_{Cu} + c_{Zn}/d_{Zn} + c_{Zr}/d_{Zr} + c_O/d_O)$, where S_{BET} is BET surface area, c_{Cu}, c_{Zn}, c_{Zr}, and c_O are the surface atomic concentrations, and d_{Cu}, d_{Zn}, d_{Zr}, and d_O are the atomic site densities which are assumed as 0.032 mmol m^{-2} (Cu), 0.077 mmol m^{-2} (Zn^{2+}), 0.070 mmol m^{-2} (Zr^{4+}), and 0.030 mmol m^{-2} (O^{2-}) on the basis of the ionic radii. Although ARSF neglects the matrix effects such as elastic-scattering correction factor and electron inelastic mean free path, the uncertainty is less than 2% [31]. Since the detection depth of XPS is few nanometers and the size of the particles comprising the catalyst is tens of nanometers, the surface information from XPS reflects the surface atomic composition of the catalyst. Hence, the Cu surface area estimated from XPS is at least semi-quantitative and available for comparison purpose. The Cu area for Cu/ZnO after the reaction for 20 min can be calculated as 2 $m^2\ g^{-1}$ and the value is kept after the reaction for 420 min. No significant change in the Cu crystallite size during the reaction for 420 min (see Table 1) also shows that the deactivation is not caused by sintering of the Cu particles at the initial stage of the reaction. The discernible decrease in the BET surface area during the reaction (see Table 2) is probably due to an increase in the crystallite size of ZnO (see Table 1). Since the mean crystallite size of metal often close to the mean particle size [32,33], one can roughly evaluate the total surface area of Cu particles without aggregation from the mean crystallite size. On the basis of the data in Table 1, the areas of Cu particles after the reaction for 20 min and 420 min are calculated as 10 and 9 $m^2\ g^{-1}$, respectively, where it is assumed that the particles are spherical and the sizes are equal to the mean crystallite sizes (the density of Cu is 8.9 g cm^{-3}). The particle areas are considerably larger than the Cu surface areas calculated from the surface concentrations and the BET surface areas; therefore, it is estimated that a large part of Cu particles are covered with zinc oxide. The shadow of particles can be seen in a lump shown in Fig. 4b and the EDS analysis (Fig. 4d) evidences that the lump is

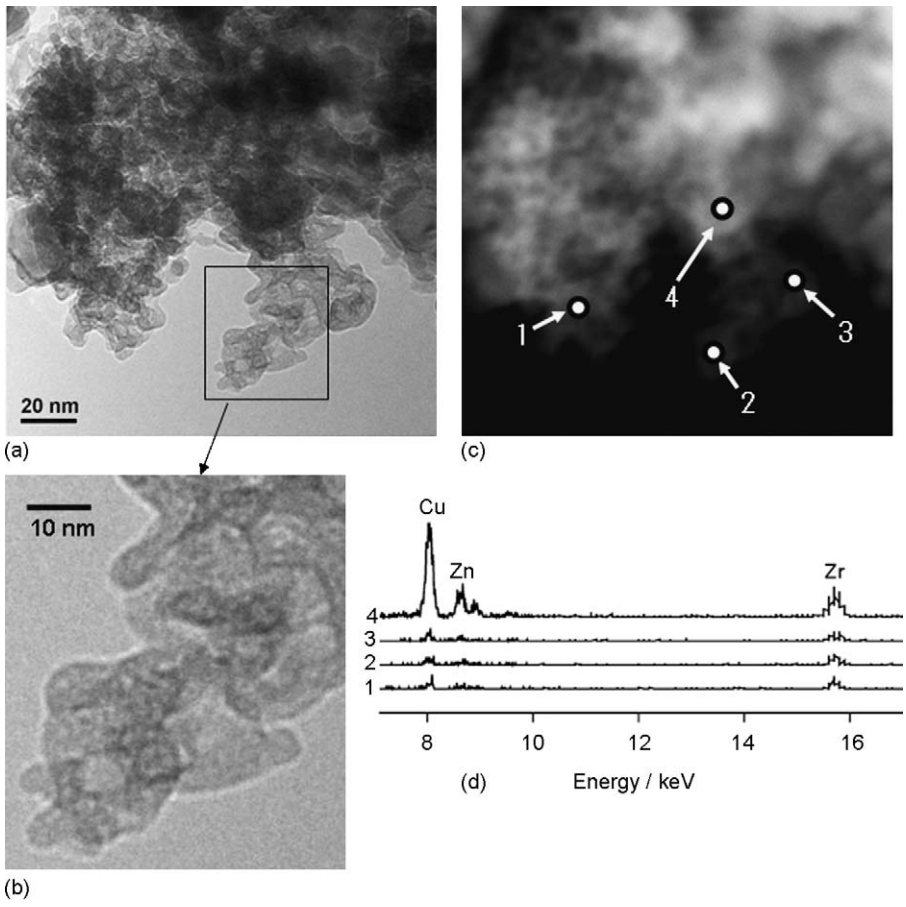

Fig. 7. TEM and HAADF/STEM images and EDS analysis of a different portion in the same aggregation of Cu/ZnO/25ZrO_2 shown in Fig. 6. (a) TEM image, (b) partial enlargement of the TEM image, (c)HAADF/STEM image, and (d) EDS spectra on points 1–4.

inhomogeneous. Hence, Cu and ZnO particles in Cu/ZnO are highly aggregated and the Cu particles are probably in strong contact with the ZnO particles.

It is reported that the heat of CO adsorption on a Cu/ZnO catalyst is lower than that on Cu/Al_2O_3, where the low adsorption heat is rationalized by the strong metal–support interaction (SMSI), i.e., adsorption of ZnO_x species on the Cu metal surface [34]. The catalytic activity of copper to methanol synthesis from hydrogen and carbon dioxide is known to increase in presence of ZnO_x species on the surface [35,36]. Günter et al. reported that dissolution of zinc atoms up to 4 mol% in Cu lattice under the reduction of Cu/ZnO with hydrogen at 250 °C [37]. Thus, the surface interaction between copper and zinc oxide is considered to affect the activity to the methanol steam reforming, which is the reverse reaction of the methanol synthesis. It is hypothesized that the deactivation during the reforming at 400 °C is associated with the growth of the ZnO particle size because the structural change will affect the interaction between copper and zinc oxide.

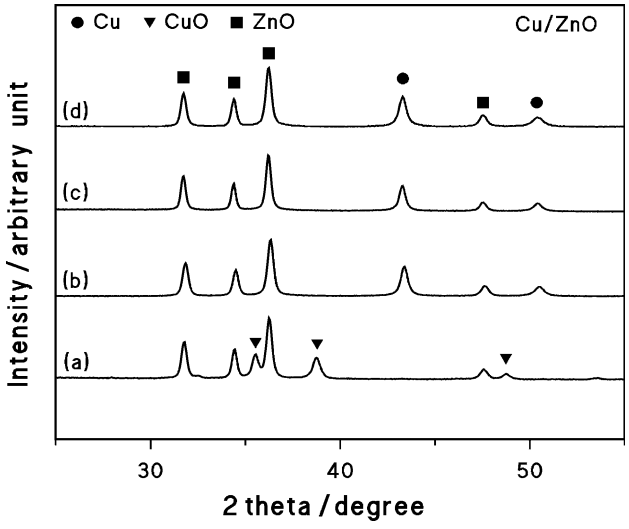

Fig. 8. XRD patterns of Cu/ZnO. (a) As prepared, (b) after the reaction for 20 min, (c) after the reaction for 420 min, and (d) reduced with hydrogen at 250 °C for 1 h.

4.2. Deactivation of Cu/ZrO_2

The broad diffraction pattern at around 33° in the XRD of Cu/ZrO_2 reduced with hydrogen suggests presence of amorphous and/or fine ZrO_2 particles (see Fig. 9d). In actual, the TEM image shows amorphous-like portions containing both Cu and Zr (see Fig. 5). Hence, fine Cu particles should be present with the amorphous-like ZrO_2. Since the intensities of the XRD peaks attributed to ZrO_2 and Cu increase with the time-on-stream without apparent line sharpening (cf. Fig. 9b and c), the amorphous-like ZrO_2 and the fine Cu particles are undetectable by XRD and they transform probably to ZrO_2 particles with the crystallite size of ca. 10 nm and Cu particles with the size of ca. 30 nm during the reaction. In the TEM image of Cu/ZrO_2 (see Fig. 5b), the small particles with the size of ca. 10 nm must be zirconium oxide; the STEM image at 3 and 4 in Fig. 5c can be regarded as that for overlapped Cu particles because the portion at 4 is significantly brighter than that at 3.

Ritzkopf et al. reported that low CO selectivity can be produced in the reforming at 300 °C or below with zirconia-supported

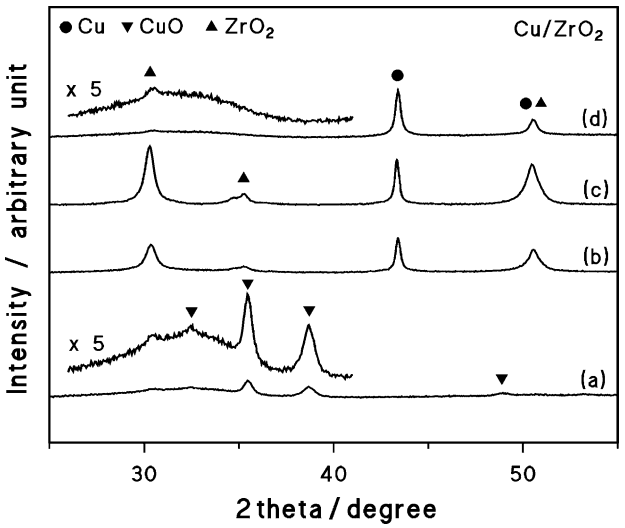

Fig. 9. XRD patterns of Cu/ZrO. (a) As prepared, (b) after the reaction for 20 min, (c) after the reaction for 420 min, and (d) reduced with hydrogen at 250 °C for 1 h.

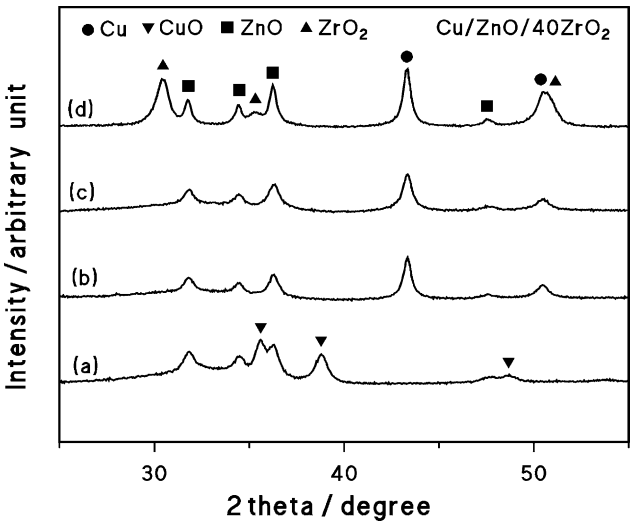

Fig. 11. XRD patterns of Cu/ZnO/40ZrO_2. (a) As prepared, (b) after the reaction for 20 min, (c) after the reaction for 420 min, and (d) after the 3rd reaction.

copper catalysts prepared by the microemulsion technique [38]. At the initial stage of the reaction with Cu/ZrO_2, the CO selectivity was significantly lower than that with Cu/ZnO (see Fig. 1). It is known that zirconium oxide stabilizes Cu^+ species in the steam reforming at 300 °C or below [38,39]. A mechanism for the reverse WGS has been proposed on copper catalysts, that is, $CO_2 + 2Cu \rightarrow CO + Cu_2O$ and $H_2 + Cu_2O \rightarrow H_2O + 2Cu$ [40]. Hence, the presence of Cu^+ species such as Cu_2O may suppress the reverse WGS and cause the low CO selectivity [41]. Since the fine Cu particles are supposed to interact with the amorphous-like ZrO_2, the low CO selectivity at the initial stage may be due to the presence of the fine Cu particles. The transformation of the fine Cu particles to those detectable by XRD can account for the deactivation and the increase in CO selectivity during the reaction.

4.3. Structure of Cu/ZnO/ZrO_2

The addition of zirconium oxide to Cu/ZnO results in the reduction of the Cu and ZnO crystallite sizes (see Table 1) and it causes the higher Cu surface area (see Table 2). Segregation of the particles is seen in Cu/ZnO/25ZrO_2 reduced at 250 °C (see Figs. 6 and 7). The amorphous-like ZrO_2 (see Fig. 7) is mostly undetectable by XRD as shown in Fig. 12e. Since the XRD peaks for ZrO_2 are unclear in the patterns for the Cu/ZnO/ZrO_2 catalysts after the reaction for 20 min (e.g. Figs. 10b, 11b, and 12b), the amorphous-like ZrO_2 exits in all the Cu/ZnO/ZrO_2 catalysts where copper and zinc oxide are probably present with the amorphous-like ZrO_2 (see Fig. 7d). The growth of the XRD peak attributed to ZrO_2 (e.g. Fig. 12) shows the crystallization of the amorphous-like ZrO_2 during the reaction, and the aggregation of Cu, ZnO, and ZrO_2 particles will be formed. On the other hand, the portion mainly comprised of copper and zinc oxide is also present in the aggregation of Cu/ZnO/25ZrO_2 (see Fig. 6), appearing that the catalyst is inhomogeneous. Since the aggregation of Cu/ZnO/40ZrO_2 is mostly homogeneous, excessive Zn probably forms the part without Zr in the process of coprecipitation.

4.4. Catalytic activity of Cu/ZnO/ZrO_2

The activity of Cu/ZnO/ZrO_2 decreases gradually with time-on-stream, but the activity at 420 min in the 1st run is significantly higher than that of Cu/ZnO (cf. Figs. 1 and 2). Hence, the addition of

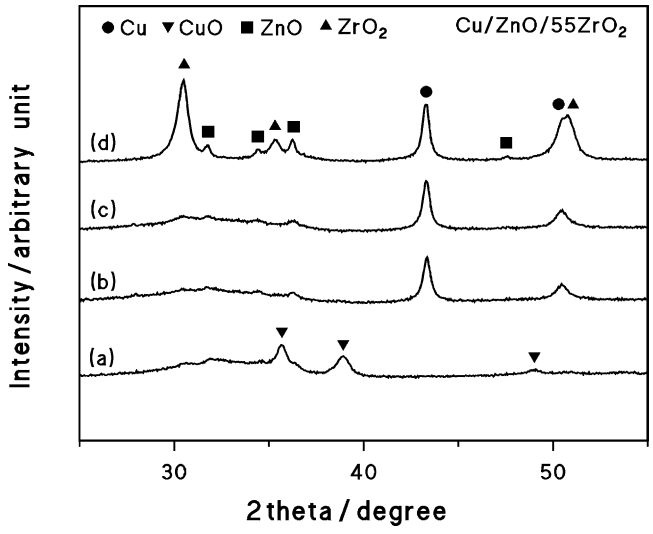

Fig. 10. XRD patterns of Cu/ZnO/55ZrO_2. (a) As prepared, (b) after the reaction for 20 min, (c) after the reaction for 420 min, and (d) after the 3rd reaction.

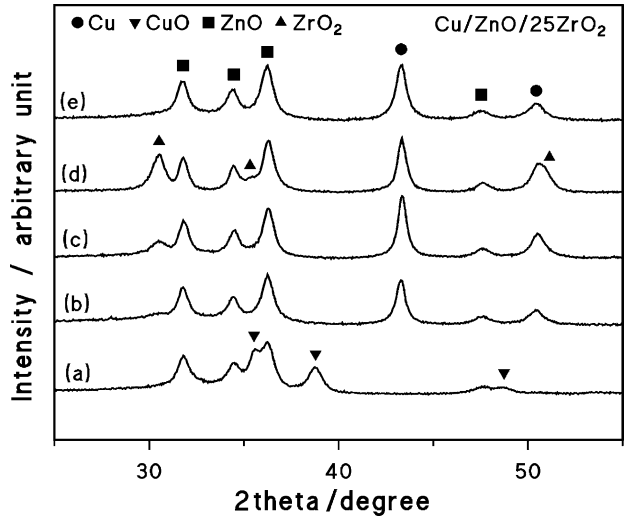

Fig. 12. XRD patterns of Cu/ZnO/25ZrO_2. (a) As prepared, (b) after the reaction for 20 min, (c) after the reaction for 420 min, (d) after the 3rd reaction, and (e) reduced with hydrogen at 250 °C for 1 h.

zirconium oxide mitigates the deactivation seen in Cu/ZnO. When F/W is too low, i.e., the contact time is long, the methanol conversion becomes close to 100% where the conversion is getting saturated and does not relate linearly to the activity. This often causes apparent stabilization of the conversion even if deactivation proceeds. In actual, the conversion of Cu/ZnO/40ZrO_2 at the F/W of 1.1 $dm^3\ min^{-1}\ g^{-1}$ is almost saturated (see Fig. 3). However, the activity at F/W of 1.6 $dm^3\ min^{-1}\ g^{-1}$ is out of the region, appearing that the conversion at this F/W depends mostly on the activity and the gradual decrease in the activity in comparison with Cu/ZnO (cf. Figs. 1 and 2) is not caused by the saturation. The selectivity to carbon monoxide increases with a decrease in the F/W even when the methanol conversion is saturated at the F/W of 1.1 $dm^3\ min^{-1}\ g^{-1}$ (see Fig. 3). This strongly suggests that the CO formation is a secondary reaction of methanol steam reforming such as the reverse WGS reaction [27,28].

A small increase in the activity is often seen at the initial stage of the 2nd and 3rd runs in comparison with the end of the previous runs (see Fig. 2). Since the catalyst was pretreated at 500 °C before the 2nd and 3rd runs, removal of surface adsorbate such as surface hydroxyl groups may occur and partially restore the activity [42]. Oxidation during the interval of the runs can be denied because the catalyst was kept under argon atmosphere. Thus, the change in the surface is partly responsible for the deactivation of Cu/ZnO/ZrO_2 during the reaction. Nevertheless, the activity is usually decreased by repeating the reaction, suggesting that the structural change of the catalyst also causes the deactivation.

Although the Cu surface areas for Cu/ZnO/40ZrO_2 and Cu/ZnO/55ZrO_2 after the 3rd runs are similar to those after the 1st runs (see Table 2), the activity decreases significantly (see Fig. 2). Since Cu/ZnO/55ZrO_2 should contain a considerable quantity of the amorphous-like ZrO_2 (see Fig. 10b), the crystallization of ZrO_2 could be responsible for the deactivation as observed with Cu/ZrO_2. However, the deactivation is not serious despite the significant crystallization after the 3rd run (see Fig. 10d). In addition, no increase in the CO selectivity is seen with Cu/ZnO/55ZrO_2 (see Fig. 2), suggesting that the crystallization is not a major reason for the deactivation.

The crystallization of ZrO_2 is simultaneously seen with the growth of ZnO particles in Cu/ZnO/40ZrO_2 and Cu/ZnO/55ZrO_2 (see Table 1). On the other hand, the size of ZnO is stable and the crystallization of ZrO_2 is gradual in Cu/ZnO/25ZrO_2, which is fairly durable. Since the change in the particle size of ZnO probably affects the interaction between copper and zinc oxide, the deactivation may be caused by the change in the interaction as discussed in Section 4.1. Although Cu/ZnO/25ZrO_2 is inhomogeneous and the portions similar to Cu/ZnO are present, the fairly stable activity suggests that the high concentration of zinc oxide is rather advantageous. The presence of ZrO_2 particles is supposed to buffer the growth of ZnO particles. The high content of zirconium oxide is considered to promote the growth of ZrO_2 particles and it may cause the growth of ZnO. Thus, the ZrO_2 content will be important in preparation of a durable catalyst.

5. Conclusions

Addition of zirconium oxide to Cu/ZnO improves the activity and stability of the copreciptated catalyst in the methanol steam reforming at 400 °C. The CO selectivity with Cu/ZnO/ZrO_2 is lower than that with Cu/ZnO, while the selectivity decreases with a decrease in the methanol conversion. The higher BET surface area can be produced by the addition of zirconium oxide. The particle sizes of Cu and ZnO for Cu/ZnO/ZrO_2 are considerably smaller than those for Cu/ZnO. Growth of the ZnO particles can be observed with Cu/ZnO after the reaction, but the presence of zirconium oxide suppresses it significantly. Although no apparent growth of Cu particles takes place in Cu/ZnO/ZrO_2 during the reaction, the activity decreases gradually with the time period of the reaction. The growth of ZnO particles may be responsible for the deactivation of the catalyst because of the change in the interaction with Cu particles.

The time-on-stream in this study is insufficient for evaluation of the long-term stability, but Cu/ZnO/ZrO_2 is a hopeful candidate. The further investigation is currently under way to improve the durability.

References

[1] Japanese Patent Kokai, 2004-292202.
[2] Y. Choi, H.G. Stenger, Appl. Catal. B 38 (2002) 259.
[3] P. Marques, N.F.P. Ribeiro, M. Schmal, D.A.G. Aranda, M.M.V.M. Souza, J. Power Sources 158 (2006) 504.
[4] C. Song, in: N. Brandon, D. Thompsett (Eds.), Fuel Cells Compendium, Elsevier, Oxford, 2005, p. 53.
[5] Y.-M. Lin, M.-H. Rei, Catal. Today 67 (2001) 77.
[6] E. Kikuchi, S. Kawabe, M. Matsukata, J. Japan Petro. Inst. 46 (2003) 93.
[7] A. Basile, G.F. Tereschenko, N.V. Orekhova, M.M. Ermilova, F. Gallucci, A. Iulianelli, Int. J. Hydrogen Energy 31 (2006) 1615.
[8] B.K.R. Nair, M.P. Harold, Chem. Eng. Sci. 61 (2006) 6616.
[9] F. Gallucci, A. Basile, S. Toshi, A. Iulianelli, E. Drioli, Int. J. Hydrogen Energy 32 (2007) 1201.
[10] A. Iulianelli, T. Longo, A. Basile, J. Membr. Sci. 323 (2008) 235.
[11] J. Han, I.-S. Kim, K.-S. Choi, Int. J. Hydrogen Energy 27 (2002) 1043.
[12] S.N. Paglieri, J.D. Way, Sep. Purif. Methods 31 (2002) 1.
[13] J. Shu, B.P.A. Grandjean, A. Van Neste, S. Kaliaguine, Can. J. Chem. Eng. 69 (1991).
[14] C. Qi, J.C. Amphlett, B.A. Peppley, J. Power Sources 171 (2007) 842.
[15] J. Jia, J. Zhou, C. Zhang, Z. Yuan, S. Wang, L. Cao, S. Wang, Appl. Catal. A 341 (2008) 1.
[16] Y. Ma, Q. Sun, D. Wu, W.-H. Fan, Y.-L. Zhang, J.-F. Deng, Appl. Catal. A 171 (1998) 45.
[17] Y.-W. Suh, S.-H. Moon, H.-K. Rhee, Catal. Today 63 (2000) 447.
[18] J. Słoczyński, R. Grabowski, A. Kozłowska, P. Olszewski, M. Lachowska, J. Skrzypec, J. Stoch, Appl. Catal. A 249 (2003) 129.
[19] F. Arena, K. Barbera, G. Italiano, G. Bonura, L. Spadaro, F. Frusteri, J. Catal. 249 (2007) 185.
[20] J. Agrell, H. Birgersson, M. Boutonnet, I. Melián-Cabrera, R.M. Navarro, J.L.G. Fierro, J. Catal. 219 (2003) 389.
[21] P.H. Matter, D.J. Braden, U.S. Ozkan, J. Catal. 223 (2004) 340.
[22] JCPDS Files, 410254, 211486, 40836, 170923, 371484, 330448, 351401, and 401037.
[23] C. Hammond, The Basics of Crystallography and Diffraction, Oxford University Press, New York, 1997, p. 145.
[24] Z.G. Wu, Y.X. Zhao, L.P. Xu, D.S. Liu, J. Non-Crystall. Solids 330 (2003) 274.
[25] C.D. Wagner, W.M. Riggs, L.E. Davis, J.F. Moulder, G.E. Muilenberg (Eds.), Handbook of X-ray Photoelectron Spectoroscopy, Perkin-Elmer, Minnesota, 1978, p. 14.
[26] C.D. Wagner,, in: D. Briggs, M.P. Seah (Eds.), second edition, Practical Surface Analysis. Auger and X-ray Photoelectron Spectroscopy, 1, John Wiley & Sons, Inc, New York, 1990, p. 595.
[27] J. Agrell, H. Birgersson, M. Boutonnet, J. Power Sources 106 (2002) 249.
[28] H. Purnama, T. Ressler, R.E. Jentoft, H. Soerijanto, R. Schlögl, R. Schomäcker, Appl. Catal. A 259 (2004) 83.
[29] B.A. Peppley, J.C. Amphlett, L.M. Kearns, R.F. Mann, Appl. Catal. A 179 (1999) 21.
[30] A. Mastalir, B. Frank, A. Szizybalski, H. Soerijanto, A. Deshpande, M. Niederberger, R. Schomäcker, R. Schlögl, T. Ressler, J. Catal. 230 (2005) 464.
[31] ISO 18118 (2004).
[32] J.W.E. Coenen, Appl. Catal. 75 (1991) 193.
[33] Y. Matsumura, K. Kuraoka, T. Yazawa, M. Haruta, Catal. Today 45 (1998) 191.
[34] R. Naumann d'Alnoncourt, M. Kurtz, H. Wilmer, E. Löffler, V. Hagen, J. Shen, M. Muhler, J. Catal. 220 (2003) 249.
[35] J. Nakamura, T. Uchijima, Y. Kanai, T. Fujitani, Catal. Today 28 (1996) 223.
[36] I. Nakamura, T. Fujitani, T. Uchijima, J. Nakamura, Surf. Sci. 400 (1998) 387.
[37] M.M. Günter, T. Ressler, R.E. Jentoft, B. Bems, J. Catal. 203 (2001) 133.
[38] I. Ritzkopf, S. Vukojević, C. Weidenthaler, J.-D. Grunwaldt, F. Schüth, Appl. Catal. A 302 (2006) 215.
[39] H. Oguchi, H. Kanai, K. Utani, Y. Matsumura, S. Imamura, Appl. Catal. A 293 (2005) 64.
[40] M.J.L. Ginés, A.J. Marchi, C.R. Apesteguía, Appl. Catal. A 154 (1997) 155.
[41] Y. Matsumura, H. Ishibe, Appl. Catal. B 86 (2009) 114.
[42] P.H. Matter, U.S. Ozkan, J. Catal. 234 (2005) 463.